Magnetic Resonance Materials in Physics, Biology and Medicine
https://doi.org/10.1007/s10334-024-01147-w

RESEARCH ARTICLE

High-resolution prostate diffusion MRI using eddy current-nulled convex optimized diffusion encoding and random matrix theory-based denoising

Zhaohuan Zhang[1,2] · Elif Aygun[1,2] · Shu-Fu Shih[1,2] · Steven S. Raman[1] · Kyunghyun Sung[1,2] · Holden H. Wu[1,2]

Received: 1 May 2023 / Revised: 12 December 2023 / Accepted: 4 January 2024
© The Author(s), under exclusive licence to European Society for Magnetic Resonance in Medicine and Biology (ESMRMB) 2024

Abstract

Objective To develop and evaluate a technique combining eddy current-nulled convex optimized diffusion encoding (ENCODE) with random matrix theory (RMT)-based denoising to accelerate and improve the apparent signal-to-noise ratio (aSNR) and apparent diffusion coefficient (ADC) mapping in high-resolution prostate diffusion-weighted MRI (DWI).

Materials and methods Eleven subjects with clinical suspicion of prostate cancer were scanned at 3T with high-resolution (HR) (in-plane: 1.0×1.0 mm^2) ENCODE and standard-resolution (1.6×2.2 mm^2) bipolar DWI sequences (both had 7 repetitions for averaging, acquisition time [TA] of 5 min 50 s). HR-ENCODE was retrospectively analyzed using three repetitions (accelerated effective TA of 2 min 30 s). The RMT-based denoising pipeline utilized complex DWI signals and Marchenko–Pastur distribution-based principal component analysis to remove additive Gaussian noise in images from multiple coils, b-values, diffusion encoding directions, and repetitions. HR-ENCODE with RMT-based denoising (HR-ENCODE-RMT) was compared with HR-ENCODE in terms of aSNR in prostate peripheral zone (PZ) and transition zone (TZ). Precision and accuracy of ADC were evaluated by the coefficient of variation (CoV) between repeated measurements and mean difference (MD) compared to the bipolar ADC reference, respectively. Differences were compared using two-sided Wilcoxon signed-rank tests ($P < 0.05$ considered significant).

Results HR-ENCODE-RMT yielded 62% and 56% higher median aSNR than HR-ENCODE ($b = 800$ s/mm^2) in PZ and TZ, respectively ($P < 0.001$). HR-ENCODE-RMT achieved 63% and 70% lower ADC-CoV than HR-ENCODE in PZ and TZ, respectively ($P < 0.001$). HR-ENCODE-RMT ADC and bipolar ADC had low MD of 22.7×10^{-6} mm^2/s in PZ and low MD of 90.5×10^{-6} mm^2/s in TZ.

Conclusions HR-ENCODE-RMT can shorten the acquisition time and improve the aSNR of high-resolution prostate DWI and achieve accurate and precise ADC measurements in the prostate.

Keywords Prostate · Diffusion MRI · Denoising · High-resolution diffusion MRI · Random matrix theory

Introduction

Diffusion-weighted MRI (DWI) is one of the key components of multi-parametric (mp) MRI for diagnosis and grading of prostate cancer (PCa) [1]. Analysis of DWI signals, such as by mapping the apparent diffusion coefficient (ADC), can provide tissue-specific physiologic and microstructural information to aid the characterization of PCa aggressiveness [1–3].

High-spatial-resolution prostate DWI (e.g., in-plane resolution $\leq 1.0 \times 1.0$ mm^2) has potential to provide finer depiction of prostate tissue and improve conspicuity of lesions with diffusion contrast [4–8], compared to standard prostate DWI with in-plane resolution limited to around 1.6×2.0 to 2.0×2.0 mm^2, and can enable ADC mapping with reduced partial volume averaging effects [9, 10], which may improve the delineation of PCa when the tumor is intermixed substantially with adjacent normal tissue and smaller imaging voxels are desired for better tumor differentiation [5,

✉ Holden H. Wu
HoldenWu@mednet.ucla.edu

1 Department of Radiological Sciences, University of California Los Angeles, 300 UCLA Medical Plaza, Suite B119, Los Angeles, CA 90095, USA

2 Department of Bioengineering, University of California Los Angeles, Los Angeles, CA, USA

Published online: 13 February 2024

10]. However, the signal-to-noise ratio (SNR) penalty with smaller voxel sizes makes it technically challenging [11], especially with the increasingly common practice of using a phased-array body coil instead of an endorectal coil for prostate MRI [12, 13]. Since standard prostate DWI at moderate in-plane resolution (e.g., 1.6×2.0 mm^2) already acquires multiple repetitions to perform signal averaging (e.g., 6–10 repetitions) to address the intrinsically low SNR [14], further increasing the number of scan repetitions to maintain SNR for higher spatial resolution may lead to prolonged exam durations.

The eddy current-nulled convex optimized diffusion encoding (ENCODE) framework is a recently proposed diffusion waveform design technique [15–17] that automatically minimizes echo time (TE) while compensating for eddy current effects from diffusion encoding gradients for any given DWI protocol. It was recently shown that ENCODE single-shot echoplanar imaging (EPI) prostate DWI [17] improved SNR by maintaining a short TE to limit T_2 signal decay while reducing eddy current-induced distortion in the prostate compared to conventional twice-refocused bipolar and monopolar DWI waveforms, especially for protocols with longer EPI readout [15, 18, 19], i.e., those associated with higher spatial resolution. On the other hand, DWI using reduced field-of-view (FOV) acquisition in the phase encoding direction has also been demonstrated to be an effective technique in limiting susceptibility-induced distortion for achieving higher spatial resolution for prostate DWI [7, 20]. This indicates that combining ENCODE with the reduced-FOV (rFOV) technique could be an advantageous DWI acquisition strategy for high-resolution prostate DWI with short TE and reduced geometric distortion due to eddy current and susceptibility effects. However, such a high-resolution DWI technique is still expected to suffer from SNR losses proportional to the reduction in voxel size (e.g., from 1.6×2.0 to 1.0×1.0 mm^2 in-plane resolution), and maintaining SNR remains a challenge.

Recently, random matrix theory (RMT)-based denoising techniques, such as Marchenko-Pastur principal component analysis (MP-PCA) [21, 22], achieved promising performance in reducing thermal noise for diffusion MRI by exploiting the redundancy of noise statistics and anatomical/functional information shared across multiple diffusion encoding strengths/directions and repeated acquisitions (i.e., signal averaging) inherent to DWI protocols [22]. Moreover, based on RMT, a data-driven threshold can be automatically determined to distinguish between the noise-only and signal-carrying components for effective denoising while preserving the underlying signals that contain anatomical and functional information [22, 23]. MP-PCA denoising of diffusion MRI has been demonstrated in multiple organs including the prostate [24], but it has not been specifically evaluated in the context of improving SNR for high-spatial-resolution (e.g., 1.0×1.0 mm^2) prostate DWI. Since ENCODE acquisition and RMT-based denoising each address the SNR limitations of high-resolution prostate DWI from the acquisition and reconstruction perspectives, respectively, the joint application of both methods may lead to further improvements in maintaining SNR. At the same time, with RMT-based denoising, the required number of scan repetitions to achieve desirable SNR can potentially be reduced. This can shorten the acquisition time and reduce sensitivity to motion in prostate DWI.

Therefore, the purpose of this study was to develop a combined ENCODE-RMT technique which can accelerate the scan and improve the SNR and robustness of ADC mapping for high-resolution (in-plane: 1.0×1.0 mm^2) prostate DWI. Specifically, the improvement in ENCODE DWI SNR with RMT-based denoising and the associated improvement in ADC mapping in terms of precision and accuracy in the prostate were quantitatively measured and evaluated, with respect to a standard-resolution clinical DWI sequence, in a pilot cohort of subjects with clinical suspicion of PCa.

Materials and methods

High-resolution ENCODE prostate DWI sequence and protocol

The high-resolution (HR) ENCODE prostate DWI protocol was designed to have the same acquisition time as the standard-resolution clinical bipolar DWI protocol used at our institution [25], with matched parameters including *b* values, diffusion directions, and repetitions for signal averaging (Table 1). To investigate scan acceleration, the HR-ENCODE prostate DWI data were retrospectively undersampled from 7 to 3 repetitions (Fig. 1). As the DWI sequences in our protocol acquired multiple b-values and diffusion directions in an inner loop and scan repetitions in an outer loop, this retrospective undersampling strategy is consistent with an accelerated DWI scan using fewer repetitions. With reduced repetitions, the effective acquisition time can be reduced from 5 min 50 s (7 repetitions) to 2 min 30 s (3 repetitions). The main difference between the HR-ENCODE DWI protocol and the standard bipolar DWI protocol was the application of outer volume suppression RF pulses in the high-resolution protocol to null the signals from tissue outside of the desired FOV centered around the prostate [26], which enabled a reduction in the phase encoding FOV (PE-FOV) to achieve an FOV of 220×124 mm^2 and an imaging matrix with higher in-plane spatial resolution of 1.0×1.0 mm^2 vs. 1.6×2.2 mm^2 in the standard full-FOV (260×216 mm^2) prostate DWI protocol while limiting B_0 inhomogeneity-induced geometric distortion [7, 20, 26].

Table 1 Sequence parameters for high-resolution ENCODE prostate diffusion MRI and clinical standard-resolution twice-refocused bipolar diffusion MRI. SPAIR: SPectral Attenuated Inversion Recovery

Parameter	High-resolution ENCODE		Standard bipolar
Echo time (TE) (ms)	**66; 73**[a]		80
b value (s/mm^2)	0, 100, 400, 800		
Repetition time (TR) (ms)	4800		
Field of view (mm^2)	220 × **124**[b]		260 × 216
Acquired resolution (mm^2)	**1.0 × 1.0**		1.6 × 2.2
Bandwidth (Hz/pixel)	**1536**		1565
Slice thickness (mm)	3.6		
Phase-encoding direction	Anterior to Posterior (A-P)		
Diffusion directions	Tetrahedral encoding		
Parallel imaging factor	2		
Partial Fourier factor	6/8		
Fat saturation method	SPAIR		
Number of slices	16–20		
Repetitions for averaging	7	3 (retrospective undersampling)	7
(Effective) Acquisition time (ms)	5:50	2:30	5:50

[a]The minimum TE achieved by the ENCODE waveform depends on gradient hardware performance limits. The TE was 66 and 73 ms on a standard-bore scanner (3T Prisma, Siemens, Germany; Gmax = 76 mT/ms; 60-cm diameter bore) and a wide-bore scanner (3T Vida, Siemens, Germany; Gmax = 55 mT/ms; 70-cm diameter bore), respectively

[b]The high-resolution ENCODE sequence used outer volume suppression RF pulses to reduce the phase-encoding field-of-view and enable image acquisition with higher in-plane spatial resolution while reducing B_0 inhomogeneity-induced geometric distortion

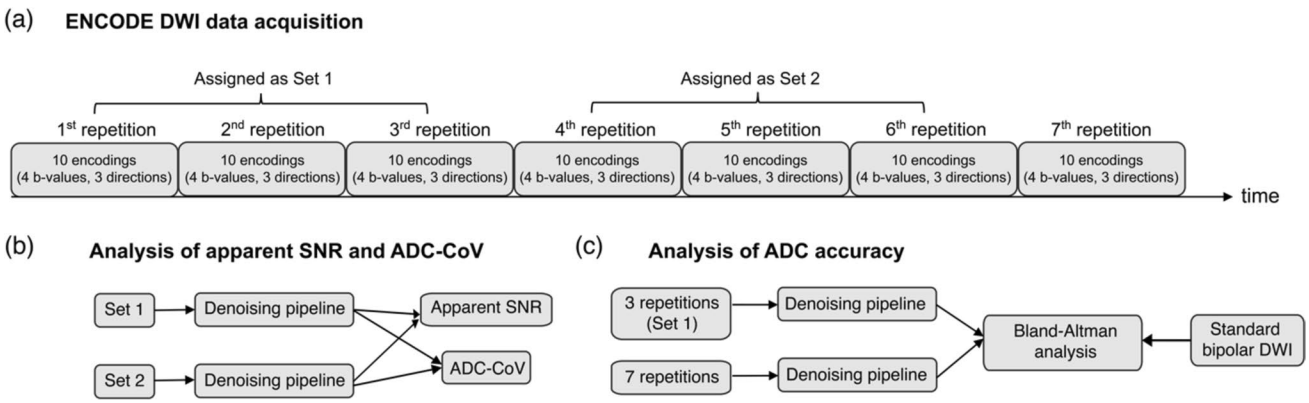

Fig. 1 **a** Diagram for the acquisition order of high-resolution (HR) ENCODE DWI data. A total of 7 repetitions were acquired in one scan. Each repetition had 10 encodings with different b-values and diffusion directions (3 for non-zero b-values). We assigned the 1st to the 3rd repetition as Set 1 and the 4th to the 6th repetition as Set 2. These 2 sets emulated 2 acquisitions using accelerated HR-ENCODE DWI. **b** Diagram showing the analysis of apparent signal-to-noise ratio (SNR) and coefficient of variation (CoV) of ADC using data from Set 1 and Set 2. **c** Diagram depicting the analysis of apparent diffusion coefficient (ADC) accuracy used in this study. HR-ENCODE-RMT ADC results from 3 and 7 repetitions were compared with ADC from standard-resolution bipolar DWI using Bland–Altman analysis

The achievable reduction in PE-FOV depended on specific peripheral nerve stimulation limits on each MRI system, and the minimal PE-FOV permitted on each scanner under a parallel imaging acceleration factor of 2 were used for HR-ENCODE DWI protocols, which reduced PE-FOV by 40% compared to standard full-FOV prostate DWI. Overall, the EPI readout duration characterized by EPI time-to-echo increased from 17 ms (full-FOV with standard resolution of 1.6 × 2.2 mm^2) to 24 ms for reduced PE-FOV (rFOV) high-resolution 1.0 × 1.0 mm^2 protocols.

Under identical gradient hardware parameters to reach a maximum b-value of 800 s/mm^2 with tetrahedral diffusion encoding [27] for high-resolution rFOV DWI protocols, the minimal achievable TE using ENCODE, conventional

twice-refocused bipolar, and conventional monopolar waveforms were 66/98/69 ms and 73/93/71 ms on one standard-bore whole-body 3 T MRI system (Gmax = 76 mT/ms, 60-cm diameter bore; Prisma, Siemens Healthineers, Erlangen, Germany) and one wide-bore whole-body 3 T MRI system (Gmax = 55 mT/ms, 70-cm diameter bore; Vida, Siemens, Germany), respectively. ENCODE achieved nearly identical or shorter TE than monopolar DWI with the additional benefit of eddy current compensation, and always reduced TE by about 20 ms compared to bipolar DWI for both scanners, highlighting the advantages of ENCODE for reducing TE (improving SNR) compared to conventional DWI sequences for high-resolution prostate DWI. For the detailed descriptions of ENCODE waveform design, we refer the readers to the prior publications [15, 17].

Theoretical and application-specific considerations for RMT-based denoising

Based on RMT, for a low rank 2D matrix contaminated by additive noise with an independent identically distributed (i.i.d.) zero-mean Gaussian distribution [21, 22], the asymptotic distribution of noise-only component singular values will follow the Marchenko-Pastur (MP) distribution [21], while the signal-carrying components will appear as "spiked" singular values falling on the right side of the bounded MP distribution. This RMT-based model of noise provides a data-driven threshold to distinguish the signal from noise components in the singular value spectrum domain for denoising using MP-PCA [22, 23].

MP-PCA has been used to denoise magnitude images in DWI and has proven to be effective for datasets with moderate SNR (e.g., > 10) [22]. However, for low SNR applications (e.g., < 5 for high-resolution DWI), applying MP-PCA on complex DWI data becomes necessary for effective denoising [28–30], as the Rician noise distribution of magnitude data no longer approximates the Gaussian distribution [31].

In addition, the choice of the dimensions (e.g., 3D or 2D) of the local spatial kernel for forming the locally low rank matrix for MP-PCA also depends on the properties of the specific dataset. In contrast to most brain DWI applications that have isotropic high resolution (e.g., 1.25^3 mm^3), prostate DWI is commonly acquired with substantially higher in-plane resolution than slice resolution [14]. This can cause larger signal intensity and phase differences across voxels along the slice direction [32]. Thus, the use of 2D local spatial kernels for denoising complex prostate DWI data with MP-PCA is more appropriate to satisfy the spatial locally low rank assumption.

RMT-based reconstruction and denoising pipeline

Inspired by prior work on RMT-based denoising [22, 28–30, 33] and motivated by the theoretical and application-specific considerations mentioned in the previous section, we designed a reconstruction, denoising, and processing pipeline for HR-ENCODE DWI (Fig. 2). The main steps in our pipeline are described below. We considered the HR-ENCODE DWI data to be a 5D matrix with dimensions of N_x by N_y in each slice, N_z slices, N_{ch} coil channels, and a total of N_{diff} different contrasts. The N_{diff} contrasts were images from all the b-values, diffusion directions, and repetitions. In this study, all the data were acquired with $N_{diff} = 30$ (i.e., 3 repetitions × [1 direction × (1 b-value = 0 s/mm^2) + 3 directions × (3 b-values = 100, 400, 800 s/mm^2)]).

1. A separate noise scan (part of the calibration scan for DWI) was used to estimate the inter-coil-channel noise covariance matrix, which was then used to de-correlate the received DWI signal and noise across coil channels in the actual acquisition through Cholesky decomposition [29, 34].
2. A 3-line navigator was used to perform linear phase correction of k-space data [35] for reducing the ghosting artifacts resulting from misalignment of odd and even EPI echoes.
3. The parallel imaging (PI) undersampled complex k-space data ($R = 2$) were Fourier Transformed to image space to generate aliased complex-valued multi-coil DW images.
4. MP-PCA denoising was performed on the aliased complex DW images. For each coil channel from each slice, images from all the b-values, diffusion directions and repetitions were first concatenated into a 3D matrix with dimensions of $N_x \times N_y \times N_{diff} = N_x \times N_y \times 30$. Then, a local patch with size $3 \times 3 \times N_{diff}$ was extracted. The spatial dimension of the local patch was flattened to form a 2D matrix with a size of $9 \times N_{diff}$. MP-PCA denoising was applied to this 2D matrix to suppress the noise. This was repeated for all the $3 \times 3 \times N_{diff}$ local patches. Because the local patches were extracted using a sliding window approach (sliding step size = 1 sample in both x and y dimensions), a voxel could be included in different local patches and have multiple denoised results. These different denoised results were averaged in each voxel. The MP-PCA denoising process was then repeated for all the N_{ch} coil channels and all N_{ch} slices. We chose a minimal local kernel size of 3 × 3 for MP-PCA to better satisfy the locally low rank assumption. This implied that we assumed the voxels at directly adjacent spatial locations (differing by 1 voxel position) to exhibit some degree of correlation. We did not choose a larger patch size such as 5 × 5, which would assume that tissue

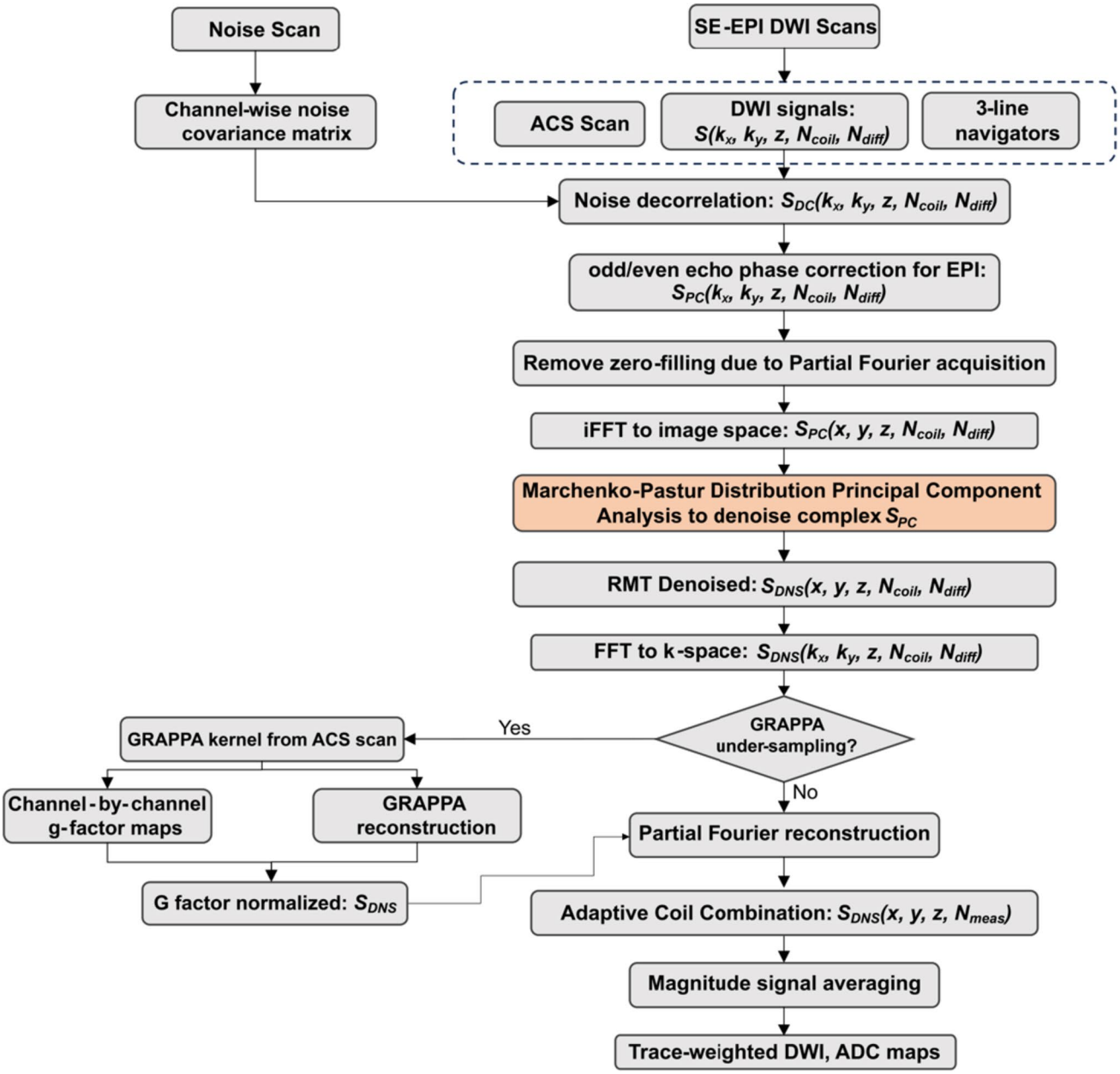

Fig. 2 Reconstruction pipeline for high-resolution ENCODE prostate DWI with random matrix theory (RMT)-based denoising. After noise decorrelation, EPI odd and even echo phase correction was applied using the 3-line navigators. The data were inverse Fourier Transformed to the image space to generate aliased images. Marchenko–Pastur distribution-based principal component analysis (MP-PCA) was applied to denoise the complex signals by utilizing the information redundancy of DWI data across different diffusion encodings including b-values/directions/repetitions. After denoising, GRAPPA parallel imaging reconstruction was performed to remove the aliasing artifacts. Partial Fourier reconstruction and adaptive coil combination were later applied to generate the final reconstructed DWI images. Averaged trace-weighted DWI and ADC maps were computed from the denoised DWI images

signals separated by two voxels were also similar. The choice of a small kernel size, such as $3 \times 3 \times 3$, was also shown to be effective in prior studies applying MP-PCA for denoising isotropic high-resolution brain DWI datasets [29, 36].

5. After MP-PCA denoising, the images were inverse Fourier Transformed to k-space for GRAPPA reconstruction [37]. Partial Fourier reconstruction and adaptive coil combination [38] were performed to combine the MP-PCA denoised multi-coil DWI data.
6. Finally, we averaged the DWI data over multiple repetitions and computed trace-weighted DWI by taking the geometrical mean over 3 orthogonal diffusion directions for $b > 0$ s/mm^2. ADC maps were calculated from DWI

using a simple least-squares fit to a mono-exponential signal decay model across DWI signals at 4 b-values (0, 100, 400, 800 s/mm^2).

Experiments

In this Health Insurance Portability and Accountability Act of 1996 (HIPAA) compliant and Institutional Review Board (IRB) approved study, 11 male subjects (age: 63 ± 11 years, body-mass index [BMI]: 25.3 ± 6.5 kg/m^2; prostate-specific antigen [PSA] levels: 5.8 ± 2.4 ng/ml) with clinical suspicion of PCa were recruited and scanned on two 3 T MRI systems using phased-array body coils. 6 subjects were scanned on a standard-bore scanner (Prisma, Siemens, Germany) and 5 subjects were scanned on a wide-bore scanner (Vida, Siemens, Germany). Scanner gradient specifications were reported in the previous section regarding ENCODE sequence design. The imaging protocol consisted of a high-resolution T_2-weighted (T2w) 2D Turbo Spin Echo (TSE) MRI sequence [25], a standard-resolution (in-plane resolution: 1.6×2.2 mm^2) clinical bipolar single-shot EPI DWI sequence used in the mpMRI protocol [25] in our institution, and the high-resolution (in-plane resolution: 1.0×1.0 mm^2) ENCODE single-shot EPI DWI sequence with identical acquisition time (TR = 4800 ms and 7 repetitions for signal averaging) and slice thickness of 3.6 mm as clinical DWI. The detailed imaging parameters for DWI are listed in Table 1. The number of activated receiver coil channels, automatically determined by the scanner for each subject, ranged from 10 to 20.

We performed our proposed RMT-based denoising reconstruction offline for (1) the HR-ENCODE datasets with 7 repetitions and (2) the retrospectively undersampled HR-ENCODE datasets with 3 repetitions (Fig. 1). For standard resolution bipolar DWI, images and ADC maps generated from the scanner were used.

Analysis and evaluation

Residual properties of RMT denoising

To validate that the proposed RMT-based denoising and reconstruction pipeline properly removed additive zero-mean Gaussian noise components with minimal removal of anatomical information, one subject was randomly chosen from the study cohort for analysis of the residuals. From this subject, the complex residuals (real and imaginary parts of DWI signals) calculated as the difference between the RMT-based denoising result (from 3 repetitions) and the input data across all receiver coil channels (e.g., 20), all 16 slices, and all diffusion encodings were pooled together ($\sim 5 \times 10^8$ data points) as a set of samples to be compared against a zero-mean Gaussian distribution. After normalization with respect to the estimated noise standard deviation (σ) calculated from all residual samples, the mean and the standard deviation of the residual distribution were reported with 95% confidence intervals.

Apparent SNR measurement in prostate zonal regions

We quantified the apparent SNR gains within the prostate peripheral zone (PZ) and transition zone (TZ) in HR-ENCODE-RMT datasets with 3 scan repetitions (Fig. 1). We used the first 3 repetitions (i.e., from the 1st repetition to the 3rd repetition) as the "first set" (s_1), and used the data from the 4th repetition to the 6th repetition as the "second set" (s_2). These two sets were processed using the proposed pipeline (Fig. 2) separately. This approach emulated repeated acquisitions using HR-ENCODE, each with 3 scan repetitions. The voxel-by-voxel apparent SNR maps for the averaged trace-weighted image with b-value of 800 s/mm^2 using HR-ENCODE DWI and HR-ENCODE DWI with RMT-based denoising (HR-ENCODE-RMT DWI) were then generated using the 2-acquisition SNR calculation equation [39]:

$$\mathrm{SNR} = \frac{\underset{r\in\mathrm{ROI}}{\mathrm{mean}}\left(s_1(r)+s_2(r)\right)}{\sqrt{2}\,\underset{r\in\mathrm{ROI}}{\mathrm{standarddeviation}}\left(s_1(r)-s_2(r)\right)}$$

The mid-gland slice of the prostate, defined as the central slice between the most superior slice containing the prostate base and the most inferior slice containing the prostate apex, was manually segmented into PZ and TZ by a prostate MRI researcher (> 6 years of experience) on the standard reconstructed $b = 0$ s/mm^2 DWI while referring to the T2w TSE MRI as an anatomical reference. The segmented PZ and TZ masks were used to extract mean SNR measurements on the evaluated $b = 800$ s/mm^2 DWI. Because this SNR measurement method relies on 2 acquisitions, we did not perform apparent SNR measurement in HR-ENCODE-RMT data with 7 repetitions.

CoV of ADC measurement in prostate zonal regions

We characterized the robustness of ADC measurements in terms of precision within prostate zonal regions. The coefficient of variation (CoV) of ADC maps from the 2 sets of HR-ENCODE acquisitions (with each set containing 3 repetitions; see previous section) was computed by taking the standard deviation of ADC estimates divided by the mean ADC estimates (Fig. 1b). Similar to region-specific SNR analysis, the mean of ADC-CoV in prostate PZ and TZ were

measured and compared between HR-ENCODE DWI and HR-ENCODE-RMT DWI.

ADC measurement in prostate zonal regions

To evaluate the accuracy of ADC measurements using HR-ENCODE-RMT DWI and HR-ENCODE DWI, the ADC measurements in prostate PZ and TZ were obtained and the agreement with the standard-resolution bipolar DWI reference was assessed. This was performed for HR-ENCODE datasets with both 3 and 7 repetitions (Fig. 1c).

Statistical analysis

For noise residual analysis of RMT-based denoising, the relationship between the log probability density of the set of residual samples ($\ln p(r)$) versus the squared sample residual magnitude (r^2) in the range of $r = 0 \sim 4\ \sigma$ was examined by performing simple linear regression, and the slope of the fitted line was reported. Note that a slope of -0.5 would indicate a perfect zero-mean Gaussian distribution.

For apparent SNR comparisons between HR-ENCODE-RMT DWI and HR-ENCODE DWI, we performed two-sided Wilcoxon signed-rank tests to compare the pair-wise differences in the median measurements over the study cohort ($N = 11$ subjects). For each subject, one mean apparent SNR measurement per PZ and TZ region at the mid-gland central slice of the prostate was extracted from HR-ENCODE DWI and HR-ENCODE-RMT DWI and used for statistical analysis. For comparisons of ADC-CoV between HR-ENCODE-RMT DWI and HR-ENCODE DWI, pair-wise differences were evaluated using two-sided Wilcoxon signed-rank tests. The same PZ and TZ regions used in the apparent SNR analysis (one mean ADC-CoV measurement per PZ and TZ region, per subject) in the subjects were used for the analysis here. For all statistical comparisons, $P < 0.05$ was considered significant.

For comparisons of mean ADC measurements in PZ and TZ, Bland–Altman analyses were conducted between HR-ENCODE-RMT DWI and standard-resolution bipolar DWI, as well as between HR-ENCODE DWI and standard-resolution bipolar DWI, using ADC measurements extracted from the same PZ and TZ regions used in the prior ADC-CoV analysis. The mean differences in zonal ADC measurements and 95% limits of agreement were reported.

Results

Residual properties of RMT-based denoising

Results of analyzing the residuals after RMT-based denoising are shown in Fig. 3. From the per-coil channel denoising residuals, there were no identifiable anatomical details, providing evidence that the proposed denoising pipeline did not remove tissue information. After fitting the pooled real and imaginary parts of the residuals to a Gaussian distribution, the distribution mean was $\mu = -0.0000$ (95% CI = [−0.0007, 0.0007]) and the normalized standard deviation was 1 (95% CI = [0.9996, 1.0004]). The linear regression analysis of the log probability density of residual samples ($\ln p(r)$) versus the squared sample residual magnitude (r^2) yielded a line with slope = −0.456 (blue line), which was close to a perfectly zero-mean Gaussian distribution with slope = −0.5 (red line). The fitted blue line had a close agreement with the reference red line in the range of $r = 0 \sim 3\ \sigma$ ($r^2 = 0$–9), and only started to deviate slightly beyond $3\ \sigma$, showing that the residuals after denoising achieved a close agreement with the zero-mean Gaussian noise statistics assumed by RMT.

Effects of RMT-based denoising on reconstructed DWI

A representative example showing the qualitative effects of RMT-based denoising for HR-ENCODE DWI at different b-values and associated ADC maps is shown in Fig. 4a. The effects of denoising were most apparent for the higher b-values of 400 s/mm^2 and 800 s/mm^2; DWI with $b = 400$ and 800 s/mm^2 appeared noisy after standard reconstruction, while RMT-based denoising yielded visually clear and sharp DWI at all b-values. This example also illustrated the downstream effects of noise suppression with RMT-based denoising, which led to improvements in the fitted ADC maps, as ADC in prostate TZ appeared brighter (higher ADC values due to reduced noise floor in DWI [40]) compared to standard reconstruction.

Apparent SNR measurement in prostate zonal regions

Representative comparisons of apparent SNR maps for HR-ENCODE DWI and HR-ENCODE-RMT DWI using data with 3 repetitions are shown in Fig. 4b. Quantitative comparison of apparent SNR differences between HR-ENCODE-RMT DWI and HR-ENCODE DWI at $b = 800$ s/mm^2 are shown in Fig. 5a. HR-ENCODE-RMT DWI yielded 62% and 56% higher median apparent SNR in PZ and TZ, respectively (PZ apparent SNR: 10.29 vs. 6.37, $P < 0.001$; TZ apparent SNR: 10.03 vs. 6.41, $P < 0.001$), for DWI at $b = 800$ s/mm^2 compared to HR-ENCODE DWI.

CoV of ADC measurement in prostate zonal regions

Representative ADC-CoV maps for HR-ENCODE DWI and HR-ENCODE-RMT DWI using 3 repetitions are shown in Fig. 4c. The overall results of ADC-CoV for HR-ENCODE

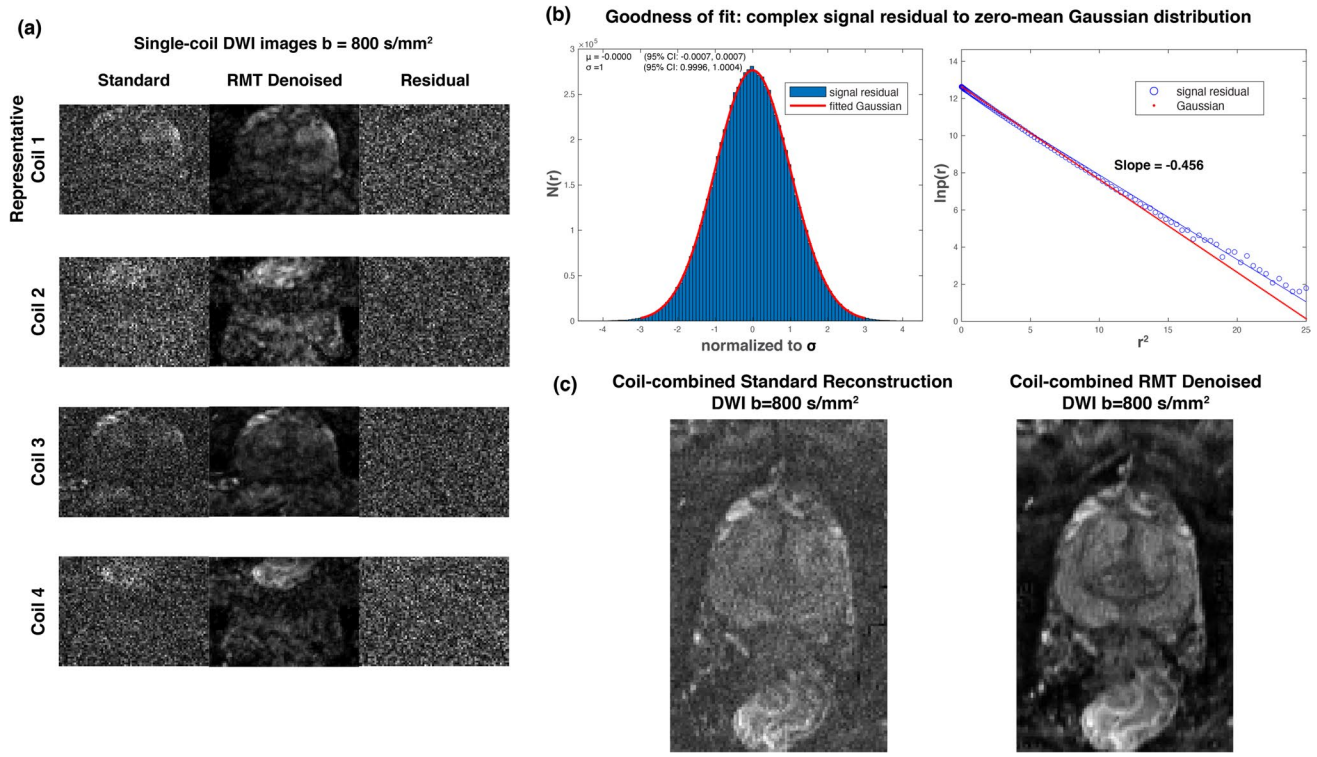

Fig. 3 Evaluation of channel-wise noise residuals after random matrix theory (RMT)-based denoising of high-resolution (HR) ENCODE prostate DWI. **a** Comparison between results from HR-ENCODE DWI using standard reconstruction and RMT-based denoising for individual coil channels. Results for DWI at $b = 800$ s/mm^2 (x direction) from 4 representative coils and the associated residuals (magnitude of the complex residual) are shown. **b** Goodness of fit for the complex residual data samples (real and imaginary parts pooled together) across all coils and slices for a zero-mean Gaussian distribution. The red reference line (slope = −0.5) indicates the ideal Gaussian distribution. **c** Comparison of the adaptive coil-combined DWI at $b = 800$ s/mm^2 using standard reconstruction and RMT-based denoising

DWI and HR-ENCODE-RMT DWI are shown in Fig. 5b. HR-ENCODE-RMT DWI reduced median ADC-CoV with respect to HR-ENCODE DWI by 63% and 70% in the PZ and TZ, respectively (PZ ADC-CoV: 0.09 vs. 0.24, $P < 0.001$; TZ ADC-CoV: 0.07 vs. 0.23, $P < 0.001$).

ADC measurement in prostate zonal regions

Representative examples of DWI and ADC maps from HR-ENCODE DWI and HR-ENCODE-RMT DWI, as well as standard-resolution bipolar DWI, are shown in Fig. 6a. Similar to the example in Fig. 4a, there was noticeable noise reduction, especially for HR-ENCODE-RMT DWI with b-value of 800 s/mm^2 compared to HR-ENCODE DWI. At the same time, the ADC map appeared darker (lower values) in the prostate TZ for HR-ENCODE DWI. After applying RMT-based denoising, the HR-ENCODE-RMT DWI ADC map became more consistent with the standard-resolution bipolar DWI ADC map, compared to HR-ENCODE DWI.

Figure 6b shows the averaged DWI signal decay curves from three techniques in prostate PZ and TZ. The mean signal decay of HR-ENCODE-RMT DWI was similar to the signal decay of standard-resolution bipolar DWI, with marked signal reduction at $b = 800$ s/mm^2. On the other hand, HR-ENCODE DWI was affected by the noise floor effect and exhibited apparent elevation of signal at $b = 800$ s/mm^2. This explains why the HR-ENCODE ADC values increased after RMT-based denoising—reducing the noise floor at high b-values will lead to higher ADC estimates through mono-exponential signal decay fitting [40].

Bland–Altman analysis of the ADC measurements from different DWI methods is shown in Fig. 7. When HR-ENCODE data with 7 repetitions were used (Fig. 7a), the HR-ENCODE-RMT ADC achieved closer agreement with standard-resolution bipolar ADC in both prostate PZ and TZ with smaller mean differences (MD) (PZ ADC MD: 9.6×10^{-6} mm^2/s; TZ ADC MD: 84.9×10^{-6} mm^2/s), compared to HR-ENCODE ADC, which had larger MD (PZ ADC MD: -278.1×10^{-6} mm^2/s; TZ ADC MD: -180.6×10^{-6} mm^2/s). When HR-ENCODE data with 3 repetitions were used (Fig. 7b), the HR-ENCODE-RMT ADC achieved smaller MD (PZ ADC MD: 22.7×10^{-6} mm^2/s; TZ ADC MD: 90.5×10^{-6} mm^2/s), compared to HR-ENCODE ADC, which had larger MD (PZ ADC

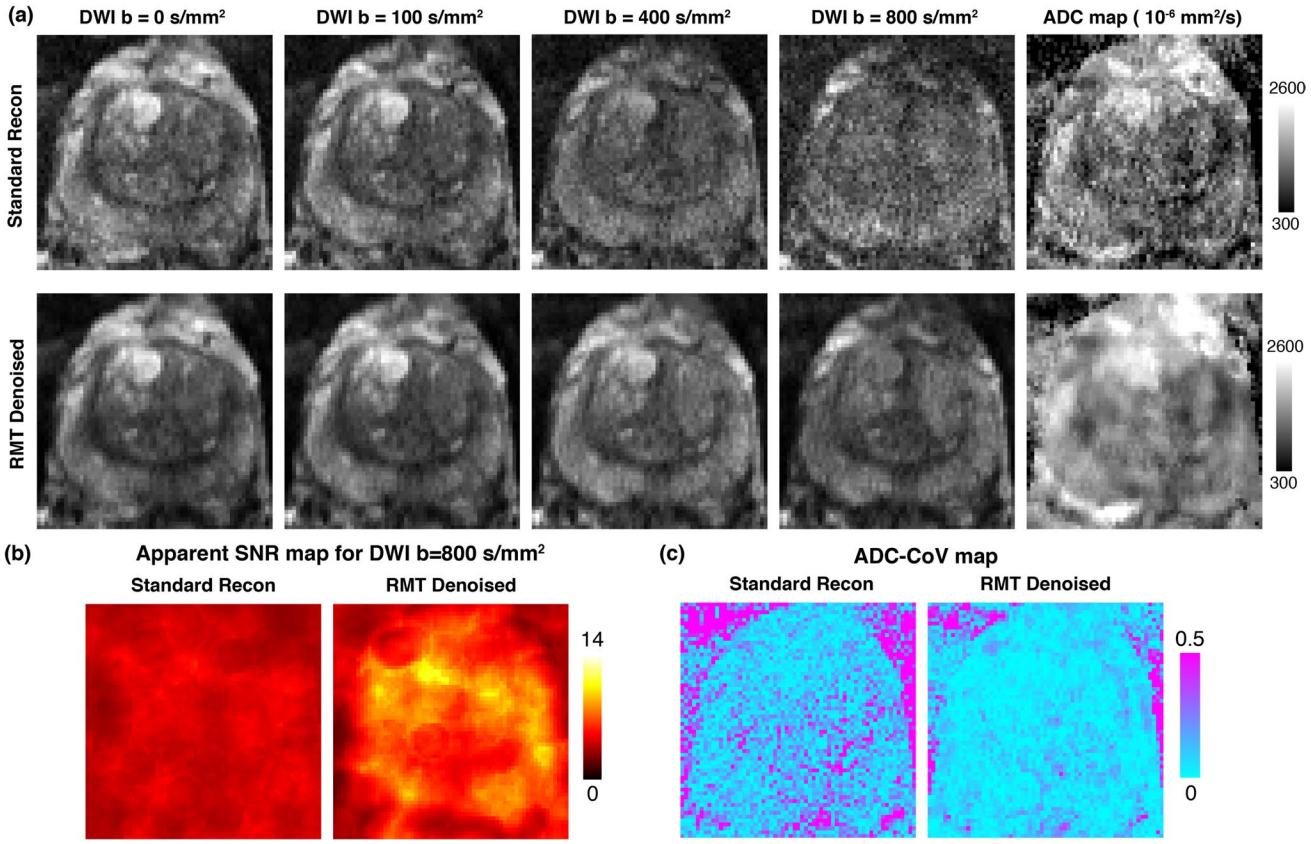

Fig. 4 **a** Comparison of high-resolution (HR) (1.0×1.0 mm^2) ENCODE prostate DWI at 4 b-values, and ADC maps using standard reconstruction and RMT-based denoising. **b** The apparent signal-to-noise ratio (SNR) maps for $b = 800$ s/mm^2 using standard reconstruction and RMT-based denoising for HR-ENCODE DWI with 3 repetitions. **c** The coefficient of variation (CoV) maps of the ADC for HR-ENCODE DWI with 3 repetitions using standard reconstruction and RMT-based denoising

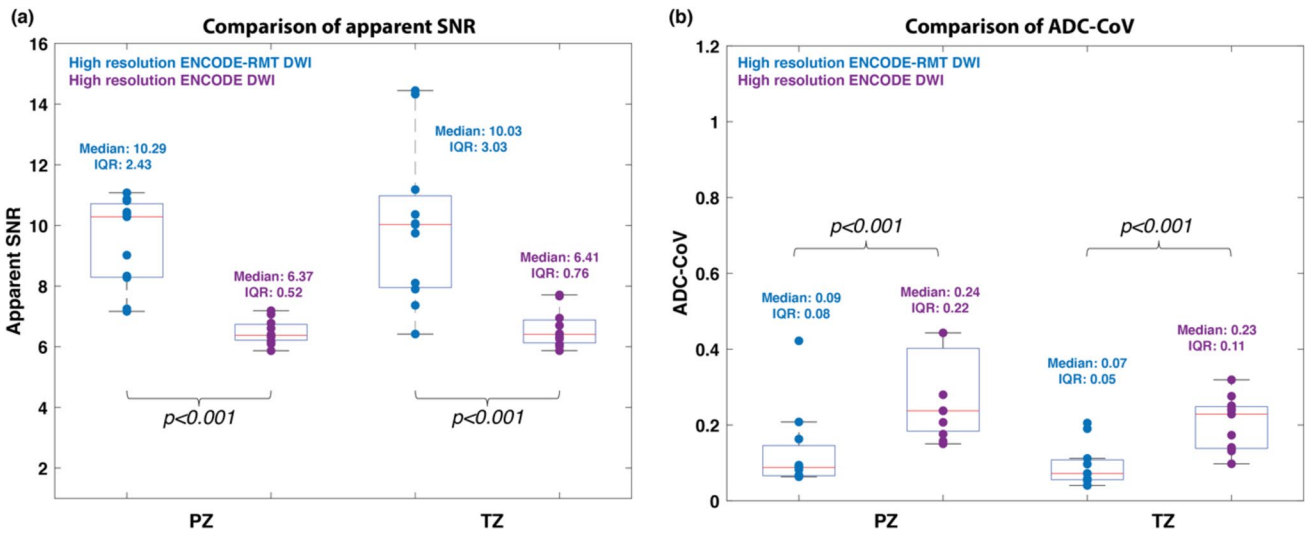

Fig. 5 **a** Comparison of mean apparent SNR of $b = 800$ s/mm^2 high-resolution (HR) (1.0×1.0 mm^2) ENCODE DWI in the prostate peripheral zone (PZ) and transition zone (PZ) using standard reconstruction and RMT-based denoising in 11 subjects. **b** Comparison of the mean ADC-CoV in prostate PZ and TZ for HR-ENCODE DWI using standard reconstruction and RMT-based denoising, as well as standard-resolution (1.6×2.2 mm^2) bipolar DWI with standard reconstruction, in 11 subjects. IQR: interquartile range

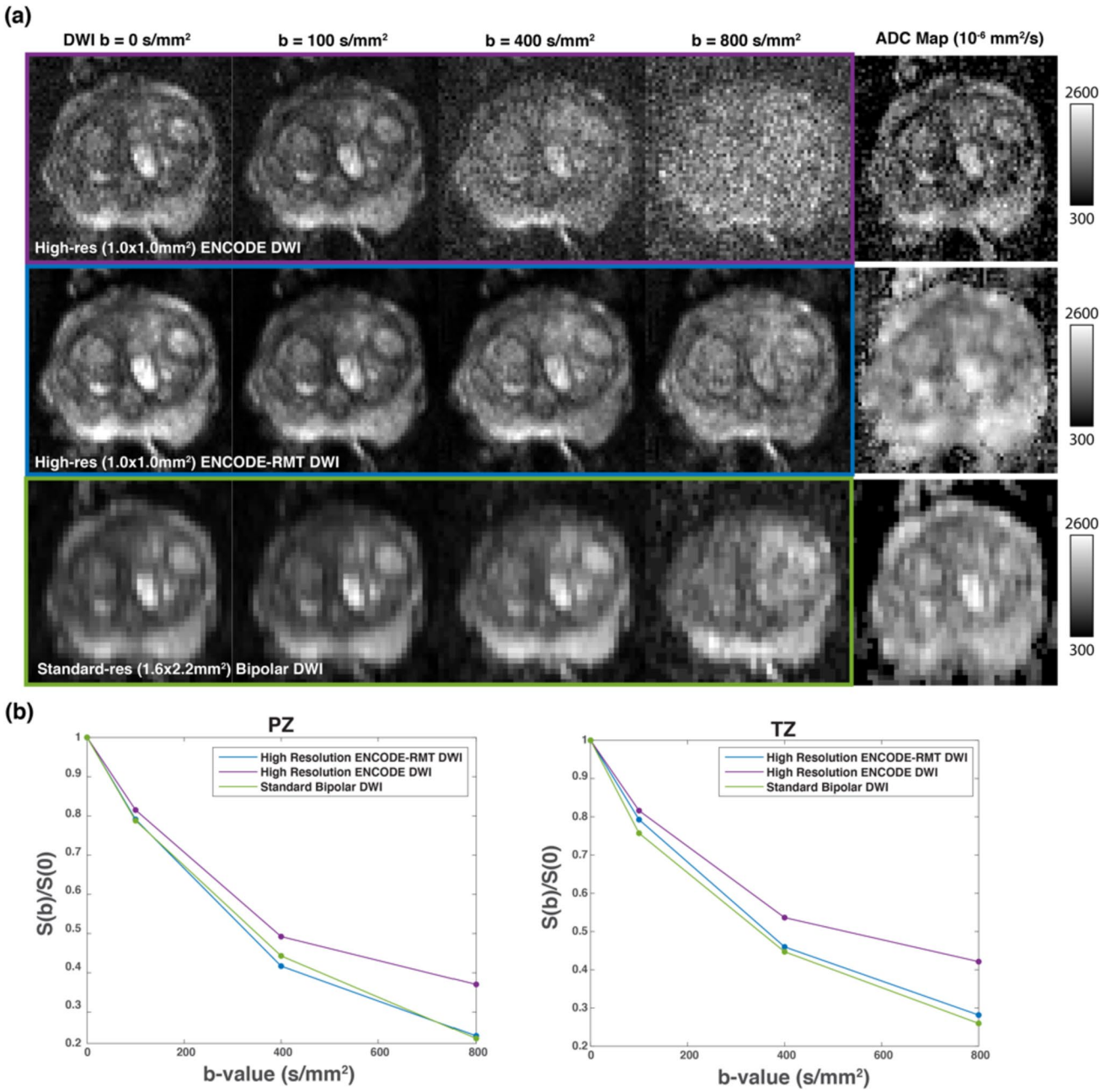

Fig. 6 **a** Comparison between high-resolution (HR) ENCODE (3 repetitions), HR-ENCODE-RMT (3 repetitions), and standard-resolution bipolar (7 repetitions) DWI and ADC map. **b** The mean diffusion-weighted signal decay curves averaged over prostate peripheral zone (PZ) and transition zone (TZ) pixels from the three techniques in the example subject. Note that the effects of the noise floor on HR-ENCODE DWI were addressed using RMT-based denoising

MD: -264.5×10^{-6} mm^2/s; TZ ADC MD: -166.5×10^{-6} mm^2/s) versus standard-resolution bipolar ADC. When the number of scan repetitions was reduced from 7 to 3, the MD in ADC between HR-ENCODE-RMT and standard bipolar DWI slightly increased. Overall, the ADC measurements from HR-ENCODE-RMT with 7 or 3 repetitions both showed low bias when compared with the standard bipolar DWI measurements.

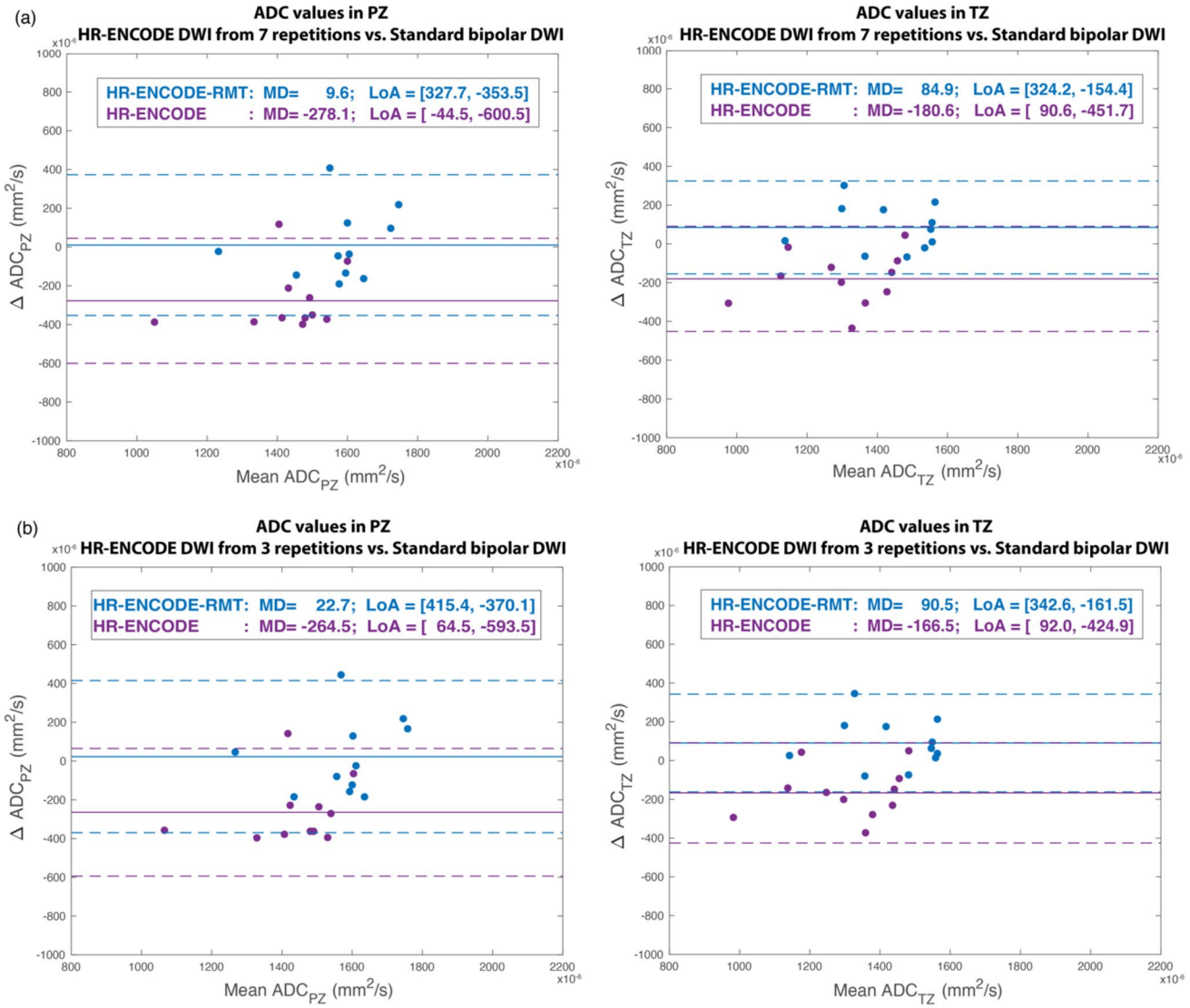

Fig. 7 **a** Bland–Altman plots comparing ADC values from high-resolution (HR) ENCODE and HR-ENCODE-RMT using 7 repetitions versus clinical standard-resolution bipolar DWI in prostate PZ and TZ. **b** Bland–Altman plots comparing ADC values from HR-ENCODE and HR-ENCODE-RMT using 3 repetitions versus standard bipolar DWI in PZ and TZ. Before denoising, HR-ENCODE with either 3 or 7 repetitions showed a large negative bias compared with standard bipolar DWI. By applying the denoising reconstruction (HR-ENCODE-RMT), the noise in larger b-values were largely suppressed and the biases were reduced. MD: mean difference. LoA: 95% limits of agreements

Representative examples

Additional representative examples of HR-ENCODE-RMT prostate DWI and standard-resolution bipolar DWI, along with a T2w 2D TSE MRI anatomical reference are shown in Figs. 8 and 9.

Discussion

The SNR of high-resolution DWI can be improved from both acquisition (e.g., diffusion encoding and TE) and reconstruction perspectives. For the most commonly used single-shot EPI DWI sequence, once the imaging parameters such as resolution, FOV, and maximum b-value are determined, the achievable SNR mainly depends on the TE of the sequence, which in turn is determined by the diffusion encoding waveforms. For the evaluated protocol, ENCODE reduced TE by ~ 20 ms compared to twice-refocused bipolar DWI, which translated to 30%-40% SNR

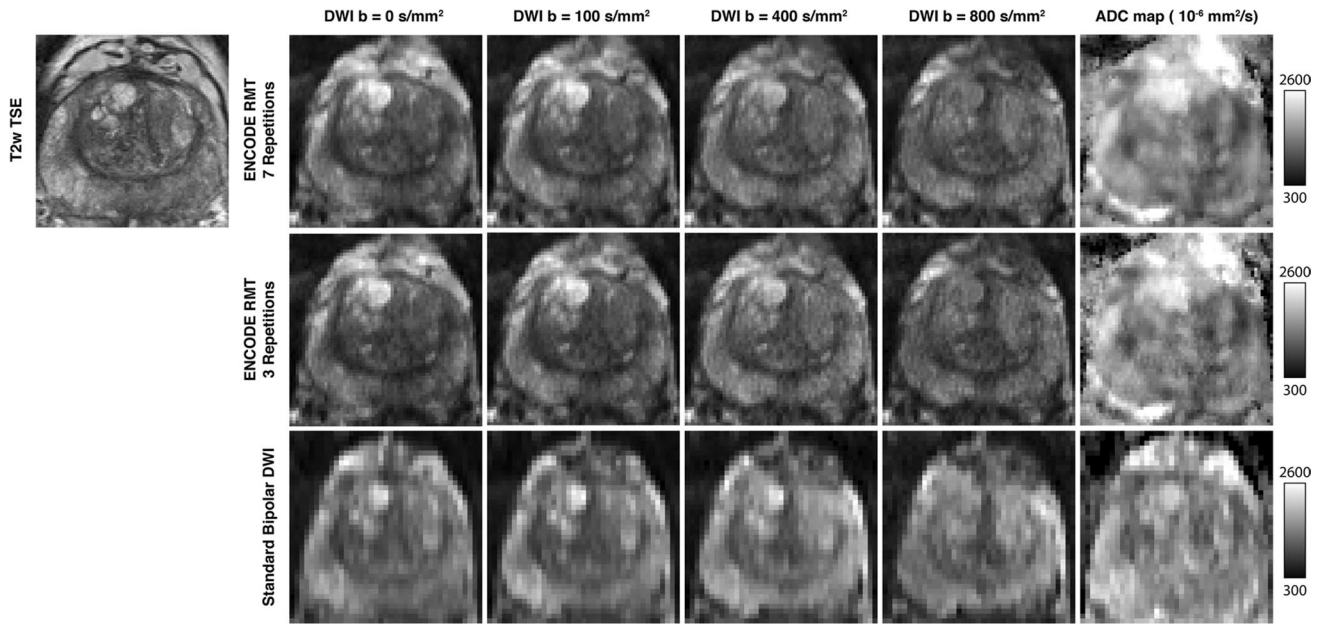

Fig. 8 Representative example of high resolution (1.0×1.0 mm^2) ENCODE-RMT prostate DWI, clinical standard-resolution (1.6×2.2 mm^2) bipolar prostate DWI, and high-resolution (0.6×0.6 mm^2) 2D T_2-weighted TSE MRI anatomical reference from a 69-year male subject (BMI = 22 kg/m^2, PSA = 6.4 ng/ml, standard-bore scanner)

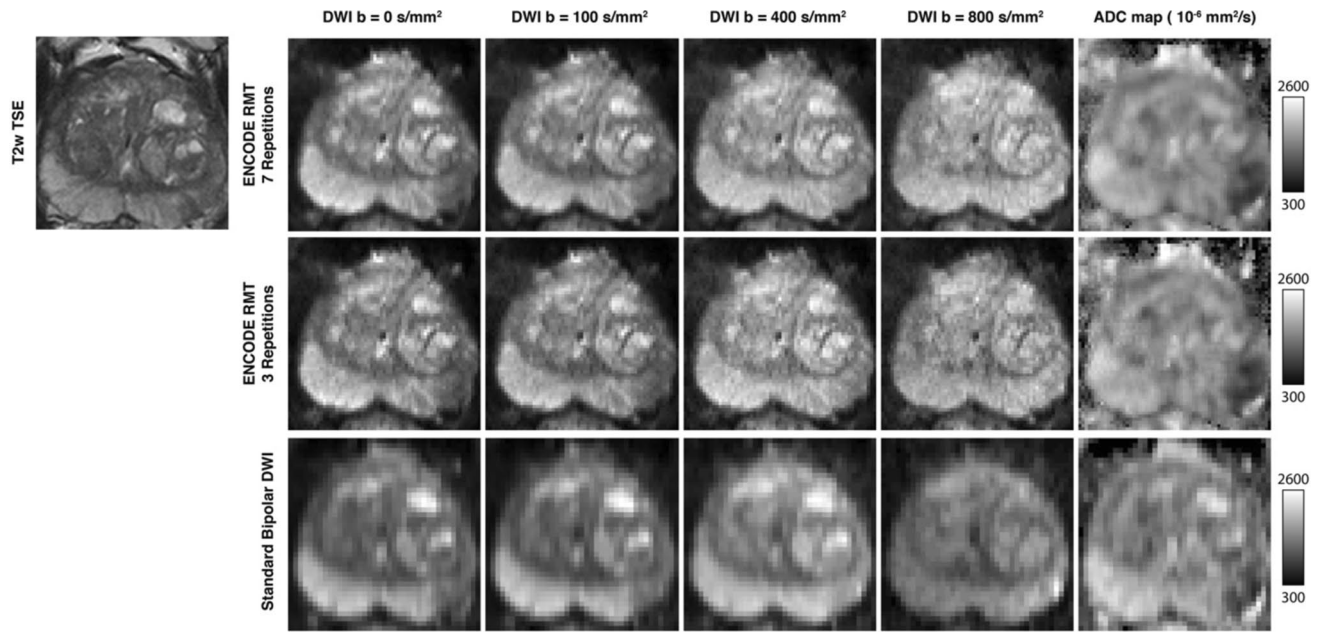

Fig. 9 Representative example of high resolution (1.0×1.0 mm^2) ENCODE-RMT prostate DWI, clinical standard-resolution (1.6×2.2 mm^2) bipolar prostate DWI, and high-resolution (0.6×0.6 mm^2) 2D T_2-weighted TSE MRI anatomical reference from a 67-year male subject (BMI = 24.9 kg/m^2, PSA = 8.8 ng/ml, wide-bore scanner)

gains based on reduced T_2 signal decay [17]. While DWI using monopolar diffusion waveforms has similarly short TE as ENCODE, monopolar DWI has the limitation of introducing eddy current-induced directionally dependent prostate distortion artifacts, which impacts the geometric fidelity of prostate DWI [17, 41, 42] unless dedicated post-processing algorithms are applied to correct for the misregistration of prostate tissue across DWI directions [41]. However, the application of post-processing algorithms for eddy current correction may interfere with the

performance of MP-PCA denoising as non-rigid registration can distort the spatial noise statistics [43] and violate the assumptions in RMT. Thus, the specific combination of TE-minimized ENCODE waveforms with RMT-based denoising is a compelling strategy to enhance the SNR of high-resolution prostate DWI while maintaining the geometric fidelity of the prostate.

The denoising and reconstruction pipeline developed in this study was built upon the original MP-PCA algorithm [22] and addressed the limitations of Rician noise floor effects in magnitude-based MRI by using complex DWI datasets [28–30, 33]. Our noise residual analysis results showed that the residuals had a close agreement with a zero-mean Gaussian distribution, therefore demonstrating the effectiveness of the proposed pipeline for specifically removing Gaussian noise. Since the evaluated prostate DWI datasets had anisotropic spatial resolution (in-plane: 1.0×1.0 mm^2; slice thickness: 3.6 mm), a local 2D spatial kernel including adjacent voxels, instead of a 3D spatial kernel (commonly used in high-resolution isotropic brain DWI datasets), was used along with the diffusion encoding dimension to form locally low-rank matrices for MP-PCA denoising. The quantitative apparent SNR analysis showed an average increase of 1.6-fold in PZ and TZ after denoising, which was similar to results reported in recent high-resolution brain DWI studies using RMT-based denoising [28, 30, 44]. Our results demonstrated that RMT-based denoising can also markedly improve SNR for high-resolution prostate DWI, despite having substantially different data acquisition conditions compared to brain DWI, such as anisotropic resolution and intrinsically lower prostate SNR using phased-array body coils.

The need to acquire multiple b-values or directions to quantify ADC and multiple scan repetitions to improve SNR can make diffusion MRI a lengthy scan. In this work, we showed the potential of using RMT-based denoising to reduce the number of scan repetitions and therefore reduce the overall acquisition time. We showed that the bias between ADC measurements from HR-ENCODE-RMT using three repetitions and standard bipolar DWI (7 repetitions) is low. This may indicate that ADC maps obtained with HR-ENCODE-RMT with a reduced acquisition time of 2 min 30 s is comparable to those of the standard bipolar DWI with an acquisition time of 5 min 50 s. The diagnostic quality of the ADC maps should be investigated in future studies through radiologist evaluation. The suitable number of scan repetitions to achieve the best trade-off between acquisition time and ADC accuracy will be investigated in the future.

For the ADC precision analysis, we used the CoV of ADC as a performance benchmark. Our results showed that the improvements in apparent SNR in HR-ENCODE-RMT DWI translated to reductions in ADC-CoV, compared to HR-ENCODE with standard reconstruction. To evaluate the ADC accuracy of the HR-ENCODE-RMT DWI, we used the standard-resolution clinical bipolar DWI sequence at our institution as a reference, since it has demonstrated stable performance both qualitatively and quantitatively in aiding the detection, diagnosis, and risk stratification of PCa as part of the clinical mp-MRI protocol of our institution [25]. A perfect agreement was not expected between ADC measurements using different techniques, even when the noise bias effects are addressed using denoising, as there are differences in TE caused by different spatial resolution parameters and diffusion encoding. Based on previous experimental and theoretical studies reporting the ADC dependency on TE and diffusion time [2, 17, 45–48] and the understanding that multiple microscopic tissue compartments in prostate tissue have distinct compartmental T_2 and ADC [9, 45–49], a $\leq$ 20% difference in ADC between bipolar DWI (TE = 80 ms) and ENCODE DWI (TE = 66 or 73 ms) estimated using a mono-exponential signal model was expected. The difference of ADC measurements between HR-ENCODE-RMT with three repetitions and standard-resolution bipolar DWI (22.7×10^{-6} mm^2/s in PZ and 90.5×10^{-6} mm^2/s in TZ) were consistent with the expected difference in ADC.

Our HR-ENCODE-RMT prostate DWI technique made distinct contributions regarding both acquisition and reconstruction to extend the nascent area of high-resolution (e.g., in-plane $\leq 1.0 \times 1.0$ mm^2) prostate DWI [5–7]. Prior high-resolution prostate DWI studies that used phased array coils (without an endorectal coil) mostly employed a maximum diffusion weighting with a moderate b-value of 500 ~ 600 s/mm^2 [6, 7], while our study employed a maximum b-value of 800 s/mm^2, which was consistent with the up-to-date Prostate Imaging – Reporting and Data System (PI-RADS) v2.1 recommendation that the acquired b_{max} should be 800 ~ 1000 s/mm^2 [50] to achieve sufficient sensitivity for low diffusivity prostate tissue such as PCa. The combination of smaller voxels and higher diffusion weighting (b-value) incurs a stronger SNR penalty for prostate DWI. Our technique combined HR-ENCODE with RMT-based denoising to overcome this more challenging imaging condition and even support potential scan acceleration (2 min 30 s) compared to standard-resolution clinical DWI (5 min 50 s). An earlier study employing an endorectal coil for high-resolution prostate DWI found no apparent SNR and image quality degradation when halving the voxel size for prostate DWI [5], which was different from the qualitative and quantitative findings in our study, where $b = 800$ s/mm^2 DWI using a phased-array body coil had low apparent SNR without denoising. This was expected as acquisitions with a phased-array body coil have substantially lower SNR than scans using an endorectal coil. Therefore, the use of an advanced denoising reconstruction method such as the

proposed RMT-based method is critical to address the SNR challenge for high-resolution prostate DWI.

Recently, advanced denoising methods such as MP-PCA [24] and deep neural networks [51] have been evaluated for enhancing the SNR of prostate DWI acquired at standard resolution (e.g., 1.6 to 2.0 mm in-plane), and showed promise for reducing the acquisition time of clinical DWI protocols by reducing the number of required averages for each b-value [24, 51]. Our study, which specifically focused on evaluating RMT-based denoising for improving the SNR of high-resolution (in-plane: 1.0×1.0 mm^2) prostate DWI, showed that advanced denoising could also be valuable for enhancing the spatial resolution and structural details of prostate DWI while maintaining SNR and ADC quantification robustness without increasing acquisition time (and even reducing acquisition time).

Although there are advantages of using complex-valued signals instead of magnitude signals in MP-PCA denoising when the data has lower SNR, a potential problem is motion-induced phase variation which can alter signal characteristics. Datasets with substantial bulk motion (i.e., shift of prostate tissue boundaries across voxels) were not analyzed in this work. However, the prostate diffusion MRI datasets that we analyzed included other effects of motion, such as shot-to-shot phase variations that occur within voxels. While our proposed denoising pipeline did not explicitly remove or correct the remaining motion-induced phase variations, our experimental results demonstrated that the RMT-based denoising approach could effectively remove noise with Gaussian distribution from complex-valued diffusion MRI datasets. This may be due to the fact that phase variations in the complex-valued signal across voxels and image contrasts are low-rank compared to the Gaussian noise components. Therefore, the RMT assumptions are still satisfied, and the noise can be separated from the multi-dimensional complex-valued signal in the spectral domain. To reduce the effects of residual phase variations in the images, we also performed magnitude signal averaging prior to trace-weighted averaging, as is often done for DWI applications. More extensive analysis of the effects of shot-to-shot phase variations on RMT-denoising performance and DWI processing can be investigated in the future.

Recent studies have shown that MP-PCA can lead to spatial resolution issues such as "leaking" across voxels [52, 53]. This can introduce image blurring and reduce the effective spatial resolution. In this work, we showed that the residual signal closely follows a Gaussian distribution. How this affects the overall image and ADC map quality could be evaluated via the local perturbation responses [52] using our proposed pipeline and our HR-ENCODE dataset. Further evaluation of the diagnostic image quality could also be conducted in the future.

In our proposed pipeline, we performed denoising before GRAPPA reconstruction. This is different from previous works that performed GRAPPA reconstruction before RMT-based denoising [30, 54]. To deal with distorted noise characteristics generated by GRAPPA, previous works used g-factor correction. However, the localized autocorrelation effects from GRAPPA cannot be fully corrected simply by g-factor correction. In our pipeline, the denoising step was applied on aliased images before GRAPPA reconstruction. The aliased images can be viewed as a superposition result of identical images with spatial shift. The effective ranks of these patches are different from the ones extracted from the unaliased images. However, the extracted patches from the aliased images are still low-rank and separable from the noise components. This is the reason why RMT-based denoising can still work on aliased images. As shown in our results, the removed noise components with respect to the aliased images were still close to Gaussian distributions. In this work, we chose to perform denoising before GRAPPA reconstruction so the influence of noise characteristics distortion from GRAPPA was avoided. Our internal investigation showed the image quality of the denoised coil-combined DW images were similar using these two pipelines (with different orders of GRAPPA and denoising). However, more thorough investigation of their differences are beyond the scope of this work. For readers' reference, the detailed pipeline of using GRAPPA before denoising can be found in Supplementary Figure S1. The corresponding denoising results are also shown in Supplementary Figure S2 (from the same subject in Fig. 3).

Our study had limitations. First, due to the limited sample size and the lack of biopsy-confirmed PCa diagnosis in all of the subjects, we did not perform lesion detection and diagnostic performance analysis of the proposed HR-ENCODE-RMT prostate DWI in comparison with standard-resolution clinical prostate DWI. The purpose and scope of this study were to evaluate the technical performance of the proposed technique in terms of apparent SNR and ADC mapping. Our results from this technical evaluation will serve as the foundation to further explore the potential benefits of high-resolution prostate DWI for PCa diagnosis. Second, in this study we only evaluated HR-ENCODE DWI using a single-shot EPI sequence with rFOV acquisition. Right now, there are alternative emerging sequences, such as readout-segmented (rs) EPI DWI [55] and diffusion-prepared bSSFP DWI [6], for achieving high spatial resolution. The choice to focus on single-shot EPI DWI was based on the fact that it remains the most widely available and commonly used DWI sequence in clinical and research settings, including for the investigation of high-resolution DWI [28, 30, 36, 51]. In addition, single-shot EPI has high scan efficiency (2- to tenfold faster acquisition per image compared to rs-EPI or diffusion-prepared bSSFP [6, 11, 55]), which facilitates

RMT-based denoising methods as MP-PCA requires a large number of diffusion encodings (> 30) to achieve sufficient redundancy in the multi-dimensional DWI dataset for separating signal from noise components. The evaluation of HR-ENCODE and RMT-based denoising for alternative DWI sequences could be a direction for future research.

Conclusion

Combining ENCODE diffusion encoding waveforms with minimized TE and random matrix theory-based denoising can accelerate and improve the signal-to-noise ratio of high-resolution (in-plane 1.0×1.0 mm^2) prostate DWI, and consequently achieved accurate and precise ADC measurements in the prostate. This technical validation study paves the way for future studies to evaluate the potential benefits of high-resolution prostate DWI for the detection and diagnosis of PCa.

Supplementary Information The online version contains supplementary material available at https://doi.org/10.1007/s10334-024-01147-w.

Acknowledgements The authors thank Nashla Barroso, Dr. Preeti Ahuja , study coordinators, and clinicians at UCLA for assisting subject recruitment. The authors thank Mayssam Wehbe, Nicholas Haid, Francine Cobla, Lalageh Arzooian, and Kelly O'Connor at UCLA for their assistance with data acquisition. The authors also thank Fadil Ali, Sevgi Gokce Kafali, and other members in the UCLA Magnetic Resonance Research Labs for helpful discussions.

Author contributions ZZ: study conception and design, acquisition of data, analysis and interpretation of data, drafting of manuscript, critical revision; EA: analysis and interpretation of data, critical revision; SS: study conception and design, critical revision, drafting of manuscript; SR: study conception and design, critical revision; KS: study conception and design, critical revision; HW: study conception and design, drafting of manuscript, critical revision.

Funding This work was supported in part by the National Cancer Institute under award number R01CA248506, the Jonsson Comprehensive Cancer Center at UCLA, and the Integrated Diagnostics Program in the Departments of Radiological Sciences and Pathology of the David Geffen School of Medicine at UCLA. The content is solely the responsibility of the authors and does not necessarily represent the official views of the National Institutes of Health.

Data availability The data that support the findings of this study are available from the corresponding author upon reasonable request.

Declarations

Conflict of interest The authors declare that there is no conflict of interest.

Ethical approval This study received Institutional Review Board approval and written informed consent was obtained from the participants.

References

1. Goh V (2023) Tumor physiology and clinically significant prostate cancer detection. Radiol Soc North Am. 306:200–201
2. Boesen L, Chabanova E, Løgager V, Balslev I, Thomsen HS (2015) Apparent diffusion coefficient ratio correlates significantly with prostate cancer Gleason score at final pathology. J Magn Reson Imaging 42(2):446–453
3. Tavakoli AA, Hielscher T, Badura P, Görtz M, Kuder TA, Gnirs R, Schwab C, Hohenfellner M, Schlemmer H-P, Bonekamp D (2023) Contribution of dynamic contrast-enhanced and diffusion MRI to PI-RADS for detecting clinically significant prostate cancer. Radiology 306(1):186–199
4. Fütterer JJ (2016) High-resolution diffusion-weighted imaging increases prostate cancer visibility? EBioMedicine 7:12
5. Medved M, Soylu-Boy FN, Karademir I, Sethi I, Yousuf A, Karczmar GS, Oto A (2014) High-resolution diffusion-weighted imaging of the prostate. Am J Roentgenol 203(1):85–90
6. Nguyen C, Sharif-Afshar AR, Fan Z, Xie Y, Wilson S, Bi X, Payor L, Saouaf R, Kim H, Li D (2016) 3 D high-resolution diffusion-weighted MRI at 3 T: Preliminary application in prostate cancer patients undergoing active surveillance protocol for low-risk prostate cancer. Magn Reson Med 75(2):616–626
7. Reischauer C, Wilm BJ, Froehlich JM, Gutzeit A, Prikler L, Gablinger R, Boesiger P, Wentz K-U (2011) High-resolution diffusion tensor imaging of prostate cancer using a reduced FOV technique. Eur J Radiol 80(2):e34–e41
8. Sharif-Afshar A-R, Nguyen C, Feng TS, Payor L, Fan Z, Saouaf R, Li D, Kim HL (2016) Prospective pilot trial to evaluate a high resolution diffusion-weighted MRI in prostate cancer patients. EBioMedicine 7:80–84
9. Bourne R, Panagiotaki E (2016) Limitations and prospects for diffusion-weighted MRI of the prostate. Diagnostics 6(2):21
10. Langer DL, van der Kwast TH, Evans AJ, Sun L, Yaffe MJ, Trachtenberg J, Haider MA (2008) Intermixed normal tissue within prostate cancer: effect on MR imaging measurements of apparent diffusion coefficient and T2—sparse versus dense cancers. Radiology 249(3):900–908
11. Wu W, Miller KL (2017) Image formation in diffusion MRI: a review of recent technical developments. J Magn Reson Imaging 46(3):646–662
12. Lee G, Oto A, Giurcanu M (2022) Prostate MRI: is endorectal coil necessary?—a review. Life 12(4):569
13. Ullrich T, Kohli M, Ohliger M, Magudia K, Arora S, Barrett T, Bittencourt L, Margolis D, Schimmöller L, Turkbey B (2020) Quality Comparison of 3 Tesla multiparametric MRI of the prostate using a flexible surface receiver coil versus conventional surface coil plus endorectal coil setup. Abdominal Radiology 45:4260–4270
14. Jambor I (2017) Optimization of prostate MRI acquisition and post-processing protocol: a pictorial review with access to acquisition protocols. Acta Radiologica Open 6(12):2058460117745574
15. Aliotta E, Moulin K, Ennis DB (2018) Eddy current–nulled convex optimized diffusion encoding (EN-CODE) for distortion-free diffusion tensor imaging with short echo times. Magn Reson Med 79(2):663–672
16. Aliotta E, Wu HH, Ennis DB (2017) Convex optimized diffusion encoding (CODE) gradient waveforms for minimum echo time and bulk motion–compensated diffusion-weighted MRI. Magn Reson Med 77(2):717–729
17. Zhang Z, Moulin K, Aliotta E, Shakeri S, Afshari Mirak S, Hosseiny M, Raman S, Ennis DB, Wu HH (2020) Prostate diffusion MRI with minimal echo time using eddy current nulled convex optimized diffusion encoding. J Magn Reson Imaging 51(5):1526–1539

18. Kyriazi S, Blackledge M, Collins DJ, Desouza NM (2010) Optimising diffusion-weighted imaging in the abdomen and pelvis: comparison of image quality between monopolar and bipolar single-shot spin-echo echo-planar sequences. Eur Radiol 20:2422–2431
19. Reese TG, Heid O, Weisskoff R, Wedeen V (2003) Reduction of eddy-current-induced distortion in diffusion MRI using a twice-refocused spin echo. Magn Reson Med 49(1):177–182
20. Attenberger UI, Rathmann N, Sertdemir M, Riffel P, Weidner A, Kannengiesser S, Morelli JN, Schoenberg SO, Hausmann D (2016) Small field-of-view single-shot EPI-DWI of the prostate: evaluation of spatially-tailored two-dimensional radiofrequency excitation pulses. Z Med Phys 26(2):168–176
21. Marchenko VA, Pastur LA (1967) Distribution of eigenvalues for some sets of random matrices. Matematicheskii Sbornik 114(4):507–536
22. Veraart J, Novikov DS, Christiaens D, Ades-Aron B, Sijbers J, Fieremans E (2016) Denoising of diffusion MRI using random matrix theory. Neuroimage 142:394–406
23. Gavish M, Donoho DL (2017) Optimal shrinkage of singular values. IEEE Trans Inf Theory 63(4):2137–2152
24. Lemberskiy G, Mazaheri Y, Vargas HA, Otazo R, Fieremans E, Novikov DS. Reducing scan time of routine prostate diffusion-weighted imaging using random matrix theory reconstruction. Processings of the 28th Annual Meeting of ISMRM. 2020
25. Johnson DC, Raman SS, Mirak SA, Kwan L, Bajgiran AM, Hsu W, Maehara CK, Ahuja P, Faiena I, Pooli A (2019) Detection of individual prostate cancer foci via multiparametric magnetic resonance imaging. Eur Urol 75(5):712–720
26. Wilm BJ, Svensson J, Henning A, Pruessmann KP, Boesiger P, Kollias SS (2007) Reduced field-of-view MRI using outer volume suppression for spinal cord diffusion imaging. Magn Reson Med 57(3):625–630
27. Padhani AR, Liu G, Mu-Koh D, Chenevert TL, Thoeny HC, Takahara T, Dzik-Jurasz A, Ross BD, Van Cauteren M, Collins D (2009) Diffusion-weighted magnetic resonance imaging as a cancer biomarker: consensus and recommendations. Neoplasia 11(2):102–125
28. Cordero-Grande L, Christiaens D, Hutter J, Price AN, Hajnal JV (2019) Complex diffusion-weighted image estimation via matrix recovery under general noise models. Neuroimage 200:391–404
29. Lemberskiy G, Baete S, Veraart J, Shepherd TM, Fieremans E, Novikov DS Achieving sub-mm clinical diffusion MRI resolution by removing noise during reconstruction using random matrix theory. In: Processings of the 27th Annual Meeting of ISMRM. 2019.
30. Moeller S, Pisharady PK, Ramanna S, Lenglet C, Wu X, Dowdle L, Yacoub E, Uğurbil K, Akçakaya M (2021) NOise Reduction with DIstribution Corrected (NORDIC) PCA in dMRI with complex-valued parameter-free locally low-rank processing. Neuroimage 226:117539
31. Gudbjartsson H, Patz S (1995) The Rician distribution of noisy MRI data. Magn Reson Med 34(6):910–914
32. Hutter J, Christiaens DJ, Schneider T, Cordero-Grande L, Slator PJ, Deprez M, Price AN, Tournier J-D, Rutherford M, Hajnal JV (2018) Slice-level diffusion encoding for motion and distortion correction. Med Image Anal 48:214–229
33. Powell E, Schneider T, Battiston M, Grussu F, Toosy A, Clayden JD, Wheeler-Kingshott CAG (2022) SENSE EPI reconstruction with 2D phase error correction and channel-wise noise removal. Magn Reson Med 88(5):2157–2166
34. Pruessmann KP, Weiger M, Börnert P, Boesiger P (2001) Advances in sensitivity encoding with arbitrary k-space trajectories. Magn Reson Med 46(4):638–651
35. Heid O. Robust EPI phase correction. Processings of the 5th Annual Meeting of ISMRM. 1997.
36. Haldar JP, Liu Y, Liao C, Fan Q, Setsompop K (2020) Fast submillimeter diffusion MRI using gSlider-SMS and SNR-enhancing joint reconstruction. Magn Reson Med 84(2):762–776
37. Breuer FA, Kannengiesser SA, Blaimer M, Seiberlich N, Jakob PM, Griswold MA (2009) General formulation for quantitative G-factor calculation in GRAPPA reconstructions. Magn Reson Med 62(3):739–746
38. Walsh DO, Gmitro AF, Marcellin MW (2000) Adaptive reconstruction of phased array MR imagery. Magn Reson Med 43(5):682–690
39. Dietrich O, Raya JG, Reeder SB, Reiser MF, Schoenberg SO (2007) Measurement of signal-to-noise ratios in MR images: influence of multichannel coils, parallel imaging, and reconstruction filters. J Magn Reson Imaging 26(2):375–385
40. Baltzer P, Mann RM, Iima M, Sigmund EE, Clauser P, Gilbert FJ, Martincich L, Partridge SC, Patterson A, Pinker K (2020) Diffusion-weighted imaging of the breast—a consensus and mission statement from the EUSOBI International Breast Diffusion-Weighted Imaging working group. Eur Radiol 30:1436–1450
41. Irfanoglu MO, Sarlls J, Nayak A, Pierpaoli C (2019) Evaluating corrections for eddy-currents and other EPI distortions in diffusion MRI: methodology and a dataset for benchmarking. Magn Reson Med 81(4):2774–2787
42. Zhang Q, Coolen BF, Versluis MJ, Strijkers GJ, Nederveen AJ (2017) Diffusion-prepared stimulated-echo turbo spin echo (DPsti-TSE): an eddy current-insensitive sequence for three-dimensional high-resolution and undistorted diffusion-weighted imaging. NMR Biomed 30(7):e3719
43. Ades-Aron B, Veraart J, Kochunov P, McGuire S, Sherman P, Kellner E, Novikov DS, Fieremans E (2018) Evaluation of the accuracy and precision of the diffusion parameter EStImation with Gibbs and NoisE removal pipeline. Neuroimage 183:532–543
44. Ramos-Llordén G, Vegas-Sánchez-Ferrero G, Liao C, Westin CF, Setsompop K, Rathi Y (2021) SNR-enhanced diffusion MRI with structure-preserving low-rank denoising in reproducing kernel Hilbert spaces. Magn Reson Med 86(3):1614–1632
45. Bourne R, Liang S, Panagiotaki E, Bongers A, Sved P, Watson G (2017) Measurement and modeling of diffusion time dependence of apparent diffusion coefficient and fractional anisotropy in prostate tissue ex vivo. NMR Biomed 30(10):e3751
46. Lemberskiy G, Fieremans E, Veraart J, Deng F-M, Rosenkrantz AB, Novikov DS (2018) Characterization of prostate microstructure using water diffusion and NMR relaxation. Front phys 6:91
47. Lemberskiy G, Rosenkrantz AB, Veraart J, Taneja SS, Novikov DS, Fieremans E (2017) Time-dependent diffusion in prostate cancer. Invest Radiol 52(7):405–411
48. Zhang Z, Wu HH, Priester A, Magyar C, Afshari Mirak S, Shakeri S, Mohammadian Bajgiran A, Hosseiny M, Azadikhah A, Sung K (2020) Prostate microstructure in prostate cancer using 3-T MRI with diffusion-relaxation correlation spectrum imaging: validation with whole-mount digital histopathology. Radiology 296(2):348–355
49. Chatterjee A, Watson G, Myint E, Sved P, McEntee M, Bourne R (2015) Changes in epithelium, stroma, and lumen space correlate more strongly with Gleason pattern and are stronger predictors of prostate ADC changes than cellularity metrics. Radiology 277(3):751–762
50. Purysko AS, Baroni RH, Giganti F, Costa D, Renard-Penna R, Kim CK, Raman SS (2021) PI-RADS version 2.1: a critical review, from the AJR special series on radiology reporting and data systems. Am J Roentgenol. 216(1):20–32
51. Kaye EA, Aherne EA, Duzgol C, Häggström I, Kobler E, Mazaheri Y, Fung MM, Zhang Z, Otazo R, Vargas HA (2020) Accelerating prostate diffusion-weighted MRI using a guided denoising convolutional neural network: retrospective feasibility study. Radiol Artif Intell 2(5):200007

52. Chan CC, Haldar JP (2021) Local perturbation responses and checkerboard tests: characterization tools for nonlinear MRI methods. Magn Reson Med 86(4):1873–1887
53. Fernandes FF, Olesen JL, Jespersen SN, Shemesh N (2023) MP-PCA denoising of fMRI time-series data can lead to artificial activation "spreading." Neuroimage 273:120118
54. Shih S-F, Zhang Z, Tasdelen B, Yagiz E, Cui SX, Zhong X, Nayak KS, Wu HH. Multi-coil multi-contrast random matrix theory-based denoising for liver fat and R2* quantification at 0.55T. Processings of the 31st Annual Meeting of ISMRM. 2023.
55. Holdsworth SJ, Skare S, Newbould RD, Guzmann R, Blevins NH, Bammer R (2008) Readout-segmented EPI for rapid high resolution diffusion imaging at 3T. Eur J Radiol 65(1):36–46

Publisher's Note Springer Nature remains neutral with regard to jurisdictional claims in published maps and institutional affiliations.

Springer Nature or its licensor (e.g. a society or other partner) holds exclusive rights to this article under a publishing agreement with the author(s) or other rightsholder(s); author self-archiving of the accepted manuscript version of this article is solely governed by the terms of such publishing agreement and applicable law.